EDGE ARTICLE

Check for updates

The large subunit of the regulatory [NiFe]-hydrogenase from *Ralstonia eutropha* – a minimal hydrogenase?†‡

Giorgio Caserta, [iD] *[a] Christian Lorent, [iD] [a] Alexandre Ciaccafava, [iD] [a] Matthias Keck,[b] Raffaella Breglia, [iD] [c] Claudio Greco, [iD] [c] Christian Limberg, [iD] [b] Peter Hildebrandt, [iD] [a] Stephen P. Cramer, [iD] [d] Ingo Zebger [iD] *[a] and Oliver Lenz [iD] *[a]

Chemically synthesized compounds that are capable of facilitating the reversible splitting of dihydrogen into protons and electrons are rare in chemists' portfolio. The corresponding biocatalysts – hydrogenases – are, however, abundant in the microbial world. [NiFe]-hydrogenases represent a major subclass and display a bipartite architecture, composed of a large subunit, hosting the catalytic $NiFe(CO)(CN)_2$ cofactor, and a small subunit whose iron–sulfur clusters are responsible for electron transfer. To analyze in detail the catalytic competence of the large subunit without its smaller counterpart, we purified the large subunit HoxC of the regulatory [NiFe]-hydrogenase of the model H_2 oxidizer *Ralstonia eutropha* to homogeneity. Metal determination and infrared spectroscopy revealed a stoichiometric loading of the metal cofactor. This enabled for the first time the determination of the UV-visible extinction coefficient of the $NiFe(CO)(CN)_2$ cofactor. Moreover, the absence of disturbing iron–sulfur clusters allowed an unbiased look into the low-spin Fe^{2+} of the active site by Mössbauer spectroscopy. Isolated HoxC was active in catalytic hydrogen–deuterium exchange, demonstrating its capacity to activate H_2. Its catalytic activity was drastically lower than that of the bipartite holoenzyme. This was consistent with infrared and electron paramagnetic resonance spectroscopic observations, suggesting that the bridging position between the active site nickel and iron ions is predominantly occupied by water-derived ligands, even under reducing conditions. In fact, the presence of water-derived ligands bound to low-spin Ni^{2+} was reflected by the absorption bands occurring in the corresponding UV-vis spectra, as revealed by time-dependent density functional theory calculations conducted on appropriate *in silico* models. Thus, the isolated large subunits indeed represent simple [NiFe]-hydrogenase models, which could serve as blueprints for chemically synthesized mimics. Furthermore, our data point to a fundamental role of the small subunit in preventing water access to the catalytic center, which significantly increases the H_2 splitting capacity of the enzyme.

Introduction

[NiFe]-hydrogenases are abundant enzymes in prokaryotes[1,2] and catalyze the reversible conversion of molecular hydrogen into protons and electrons.[3,4] These metalloproteins display a bipartite architecture that provides the necessary

[a]*Institut für Chemie, Technische Universität Berlin, Straße des 17. Juni 135, 10623 Berlin, Germany. E-mail: giorgio.caserta@tu-berlin.de; ingo.zebger@tu-berlin.de; oliver.lenz@tu-berlin.de*

[b]*Department of Chemistry, Humboldt-Universität zu Berlin, Brook-Taylor-Straße 2, 12489 Berlin, Germany*

[c]*Department of Earth and Environmental Sciences, Milano-Bicocca University, Piazza della Scienza 1, 20126 Milan, Italy*

[d]*SETI Institute, 189 Bernardo Ave., Mountain View, CA 94043, USA*

† In memory of Maurizio Bruschi.

‡ Electronic supplementary information (ESI) available: Control experiments. See DOI: 10.1039/d0sc01369b

infrastructure for the controlled interchange of substrates and products between the protein surface and the deeply buried catalytic center (Fig. 1). The large subunit of [NiFe]-hydrogenases harbors the catalytic nickel–iron site in addition to a gas channel network and a proton translocation pathway. The small subunit contains one to three iron–sulfur clusters, which can have different compositions, but always serve as an electron relay connecting the active site with the physiological electron acceptors/donors. In the absence of the physiological electron acceptors/donors, hydrogenase activity can be assayed by using artificial redox partners, such as methyl viologen or methylene blue. The site where these compounds interact with the electron transport chain, however, remains unclear.

To elucidate whether the small subunits serve merely as electronic wires or provide additional functions that support hydrogenase activity, it appears appropriate to investigate [NiFe]-hydrogenase large subunits independently from their
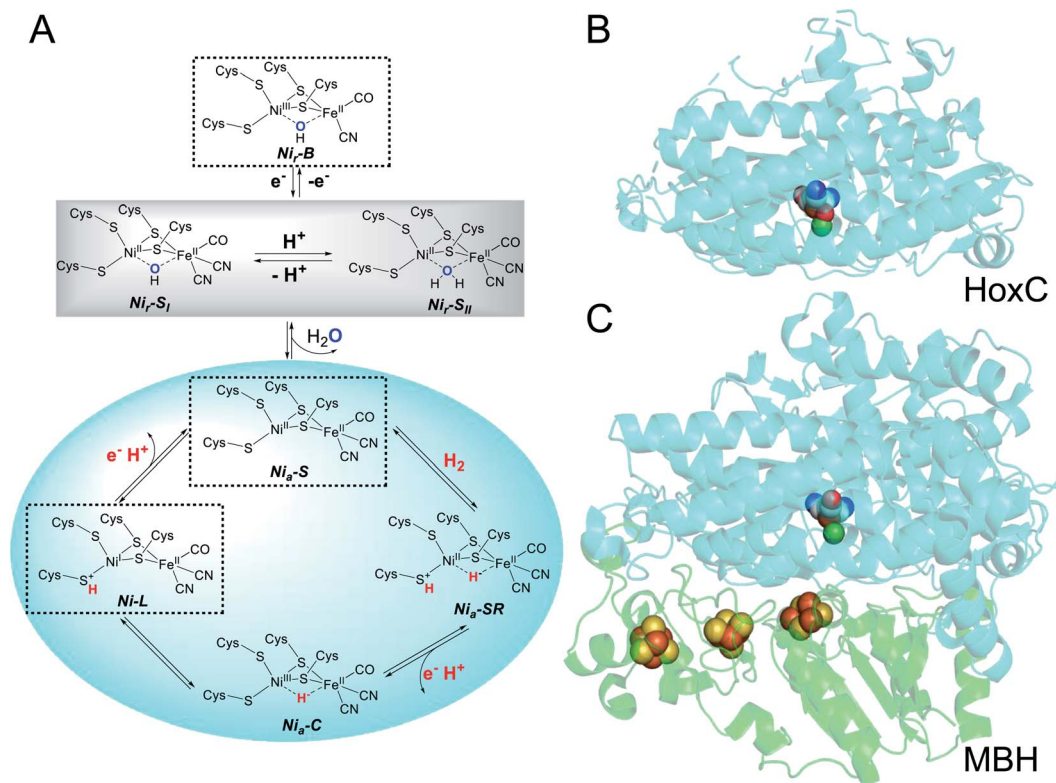
Fig. 1 Structure of a [NiFe]-hydrogenase and proposed active site states. (A) Schematic representation of the ready (subscript "r") and active (subscript "a") states of the active site (as the Ni-L state has so far not been approved to belong to the catalytic cycle, it is not labelled with a subscript "a"). The grey box comprises the interconvertible states observed for HoxC$_{ai}$. Dashed boxes indicate states identified in native RH and its isolated large subunit HoxC. (B) Homology model of HoxC generated by using the PHYRE2 protein fold recognition server (http://www.sbg.bio.ic.ac.uk/~phyre2/html/page.cgi?id=index). The MBH large subunit HoxG from *R. eutropha*, which shares 34% amino acid identity with HoxC, served as the template (3RGW). (C) Overall structure of the membrane-bound [NiFe]-hydrogenase of *R. eutropha*. The catalytic center and [FeS] clusters are depicted as spheres. The large and small subunits are depicted in cyan and green, respectively. Element color code of the cofactors: Fe, brown; Ni, green; S, yellow; C, grey; N, blue; and O, red.

counterparts. In fact, we have previously analyzed by biochemical and spectroscopic means the isolated precursor of the large subunit, preHoxG, of the O$_2$-tolerant membrane-bound [NiFe]-hydrogenase (MBH) of *Ralstonia eutropha*.[5] The protein was capable of H$_2$ activation – even in the presence of O$_2$ –, but only a restricted number of the active site redox states known to contribute to the catalytic cycle have been observed. While this study clearly provided first evidence for H$_2$ conversion without the small subunit, the results could not be generalized because of two constraints. First, the active site contained a sub-stoichiometric amount of nickel, and, second, the large subunit was still equipped with the typical C-terminal extension, which is usually cleaved off upon insertion of the catalytic center.[5] In fact, the crystal structure of the premature hydrogenase large subunit, HyhL, from *Thermococcus kodakarensis* suggests the displacement (relative to the situation in the holoprotein) of one of the four cysteines coordinating the catalytic nickel–iron site because of the presence of the C-terminal extension.[6] Recent experiments conducted to unravel the chaperone function of the C-terminal extension of the *Escherichia coli* [NiFe]-hydrogenase 2 large subunit precursor support this assumption.[7]

In the present study, we focused our attention on the large subunit of the regulatory hydrogenase (RH) from *R. eutropha*, which belongs to the small subgroup of [NiFe]-hydrogenases whose large subunits do not possess a C-terminal extension.[8] The RH contains an otherwise standard-like catalytic center (Fig. 1), in which a nickel and an iron ion are bridged by two cysteines. Two further cysteines act as terminal ligands to Ni, while one CO and two CN$^-$ ligands complete the coordination sphere of Fe. This results in a NiFe^{II}(CO)(CN)$_2$ configuration of the active site, in which only nickel changes its redox state in response to treatment of the enzymes with natural and artificial oxidants/reductants. The RH has already served as a "model" for a number of mostly spectroscopic studies including electron paramagnetic resonance (EPR), infrared (IR), and resonance Raman (RR) spectroscopy.[9–13] This is because of the apparent simplicity of the RH which can be selectively trapped in certain redox states of the active site. In its as-isolated form, the catalytic center resides in a Ni^{II}-(–)-Fe^{II}(CO)(CN)$_2$ configuration (with (–) indicating a vacant bridging position between the two metals) known as the Ni$_a$-S state, whose structure has been recently confirmed *via* X-ray crystallography.[14] Upon treatment with H$_2$, the active site adopts predominantly the Ni$_a$-C state

characterized by a bridging hydride $(Ni^{III}-(H^-)-Fe^{II}(CO)(CN)_2)$.[9] Illumination at cryogenic temperatures converts the Ni_a-C state into the Ni-L state,[15] which is discussed to be an intermediate of the catalytic cycle (Fig. 1).[16] The first known intermediate upon H_2 incubation, Ni_a-SR $(Ni^{II}-(H^-)-Fe^{II}(CO)(CN)_2)$, represents a state commonly found in "standard" [NiFe]-hydrogenases, but it is not accumulated in large amounts in RH.[12,13] The same is true for the Ni_r-S and Ni_r-B states carrying an OH^- ligand in the bridging position, which is supposed to derive from either H_2O or O_2 (Fig. 1). The apparent lack of these oxidized states has been considered to be a consequence of the O_2 tolerance of the RH.[17]

Apart from the catalytically active large subunit HoxC, the RH also includes the small subunit HoxB, which carries three [4Fe–4S] clusters. Previous experiments already showed that the HoxC subunit can be isolated without HoxB. However, the purified protein was only substoichiometrically (∼50%) loaded with nickel and thought to be redox-inactive.[18,19]

Here, we resumed our previous investigations on isolated HoxC, thereby aiming for a protein equipped stoichiometrically with the $NiFe^{II}(CO)(CN)_2$ cofactor. By adapting a new cultivation protocol for the HoxC-overproducing strain we succeeded in purifying a homogeneous protein, which turned out to be capable of H_2 activation. Moreover, the optimized protein preparation allowed for a unique spectroscopic view of the catalytic center of the [NiFe]-hydrogenase, which in the native enzyme is blurred by the spectral contributions of the iron–sulfur clusters present in the small subunit in the case of UV-visible, Mössbauer, RR, and nuclear resonance vibrational spectroscopy. On the basis of the unusual catalytic and spectroscopic properties of the isolated large subunit, we were able to derive important information on the role of the small subunit in the function of [NiFe]-hydrogenases.

Experimental

Bacterial strains and cultivation

Strains *R. eutropha* HF574(pGE537)[18] and *R. eutropha* HF574(pGE567)[17] were used for overproduction of RH (composed of single copies of HoxC and C-terminally truncated HoxB carrying Strep-tag II at the C-terminus) and isolated HoxC (carrying Strep-tag II at the N-terminus). A basic mineral medium containing H16 buffer (25 mM Na_2HPO_4, 11 mM KH_2PO_4 pH 7.0) supplemented with mineral salts (37.5 mM NH_4Cl, 1 μM $NiCl_2$, 18 μM $FeCl_3$, 68 μM $CaCl_2$ and 810 μM $MgSO_4$) was used. *R. eutropha* pre-cultures were grown for 48 h at 30 °C and 120 rpm in the basic mineral medium containing 0.4% fructose and 22.5 μM tetracycline. In contrast to a previous, less time-consuming, but more aerobic cultivation strategy,[18] main cultures were grown in baffled Erlenmeyer flasks filled to 80% of their capacity with the basic mineral medium containing with 0.05% fructose, 0.4% glycerol and 22.5 μM tetracycline. Upon inoculation with pre-culture, the cultivation was performed at 30 °C and 120 rpm until the optical density at 436 nm reached a value of 11–13. The cells were harvested by centrifugation (11 500 × *g*, 4 °C, 15 min), and the cell pellet was flash frozen in liquid nitrogen and stored at −80 °C until further use. Mineral medium for production of [^{57}Fe]-labelled HoxC contained $^{57}FeCl_3$ instead of $^{56}FeCl_3$ with natural isotope distribution.

Protein purification

The cell pellets were resuspended in lysis buffer (3–5 mL of buffer per g of cell paste) consisting of 50 mM Tris–HCl, pH 8.0, 150 mM NaCl, protease inhibitor cocktail (completely EDTA-free, Roche) and DNase I (Roche). The cells in the resulting suspension were disrupted in a French pressure cell (G. Heinemann Ultraschall and Labortechnik, Schwäbisch Gmünd, Germany) at 1.24×10^8 Pa (18 000 psi). The crude extracts were ultracentrifuged (100 000 × *g*) for 40 min at 4 °C, and the soluble fraction was loaded onto a Strep-Tactin high-capacity column (IBA, Göttingen, Germany). The column was washed with ten bed volumes of washing buffer (50 mM Tris–HCl, pH 8.0, 150 mM NaCl), and the proteins were eluted with 4 bed volumes of 50 mM Tris–HCl, pH 8.0, 150 mM NaCl and 3 mM D-desthiobiotin. The eluted proteins were concentrated by ultrafiltration (4000 × *g*, 4 °C) using Amicon Ultra Ultracel 30 kDa cut-off concentrators (Millipore). The resulting protein solution was mixed with 20 bed volumes of 50 mM Tris–HCl, pH 8.0, 150 mM NaCl and concentrated again by ultrafiltration. The final concentrate was flash-frozen in liquid nitrogen and stored at −80 °C. Size-exclusion chromatography analysis of HoxC was performed on a Superdex S 200 Increase 10/300 GL column using a buffer composed of 50 mM Tris–HCl, pH 8.0, 150 mM NaCl. Protein standards were run under the same conditions to establish a calibration curve. The protein concentration was determined using a Pierce BCA Protein Assay kit (Thermo Scientific). A solution of bovine serum albumin served as the standard. The protein purity was assessed by SDS-PAGE and subsequent Coomassie Brilliant Blue G-250 staining. Immunological detection of HoxC was carried out as described before.[18] Polyclonal antibodies obtained against RH were used for HoxC and RH detection. Alkaline phosphatase-labelled goat-anti-rabbit IgG (Dianova, Hamburg, Germany) was used as secondary antibody.

Metal content analysis

The nickel and iron content of HoxC was determined by using an inductively coupled plasma optical emission spectrometer (ICP-OES Optima 2100, PerkinElmer), taking Ni and Fe traces in the purification buffer into account. Three samples each containing 500 μL of 10 μM HoxC solution were used for the metal content analysis.

Activity assays

H_2 oxidation. H_2-Mediated reduction of methylene blue was measured spectrophotometrically using a Cary 50 UV-vis spectrophotometer (Varian, Agilent, Santa Clara, California) as previously described.[20] The reaction was performed in a glass cuvette (1 cm path length) at 30 °C. The 2.0 mL reaction contained a buffer mixture of 50 mM K_2HPO_4 and 100 mM citric acid (pH 5.0–8.0) and 0.2 mM methylene blue. Upon saturation of the mixture by bubbling with H_2 gas, the protein sample was injected using a gas-tight Hamilton syringe. H_2-dependent

reduction of the dye was carried out at 570 nm using a molar extinction coefficient of 13.1 mM^{-1} cm^{-1}. Measurements were repeated in triplicate using two different protein samples.

Catalytic H/D exchange reaction. D_2 and HD production rates were calculated upon enzymatic uptake of H_2 in D_2O-based buffer. The amount of D_2 and HD gases was measured in a modified O_2 electrode chamber (DW2/2, Hansatech, King's Lynn, U.K.) connected by a homemade brass adaptor to a mass spectrometer (OmniStar G3D 301 T3 Quadrupole, Pfeiffer Vacuum, Berlin, Germany). The measured mass-to-charge ratios (m/z) for H_2, HD and for D_2 were 2, 3 and 4 respectively, and the mass spectrometer settings have been described previously.[21] The reaction chamber was separated from the vacuum side of the mass spectrometer by a gas-permeable Teflon membrane (12.5 μm, Hansatech). The reaction volume was 1.9 mL, and the measurement was performed at room temperature under continuous stirring at 1250 rpm. The reaction buffer contained 50 mM K_2HPO_4/100 mM citric acid in D_2O (pH 3.0–9.0) and was bubbled with H_2 gas until saturation. Then, protein samples were injected using a gas-tight Hamilton syringe. D_2 and HD production rates were monitored, and data analysis was performed as described previously.[21]

Spectroscopy

UV-visible spectroscopy. UV-visible absorption spectra have been measured using a Cary 300 UV-vis spectrophotometer (Varian, Agilent, Santa Clara, California). The spectra were obtained between 250 and 800 nm using washing buffer (50 mM Tris–HCl pH 8.0, 150 mM NaCl) as a reference for the baseline. HoxC spectra were acquired using 200 μM and 15 μM protein solutions.

Infrared (IR) spectroscopy. HoxC and RH protein solutions were transferred into a gas-tight, homemade, temperature controlled (10 °C), transmission cell equipped with two sandwiched CaF_2 windows, separated by a Teflon spacer (optical path length of 50 μm). Spectra with a 2 cm^{-1} resolution were recorded on a Tensor 27 Fourier-transform spectrometer from Bruker equipped with a liquid nitrogen cooled mercury cadmium telluride (MCT) detector. Thereby, 200 scans were averaged for a single spectrum. The sample compartment was purged with dried air. A buffer spectrum (50 mM Tris–HCl 8.0, 150 mM NaCl) was chosen as a reference to calculate the corresponding absorbance spectra. Bruker OPUS software 7.5 was used for data evaluation and Origin 2018b for preparation of the figures. The HoxC and RH samples were analyzed in a concentration range of 0.5–1.0 mM and 0.2–0.4 mM, respectively. The HoxC samples used for pH studies have been equilibrated at the desired pH using a buffered solution of 100 mM K_2HPO_4 and 50 mM citric acid. $K_3Fe(CN)_6$ ($E^{0\prime} = 0.420$ V *vs.* SHE at pH 8.0),[22] $Na_2S_2O_4$, and K_2IrCl_6 ($E^{0\prime} = +0.96$ V *vs.* SHE at pH 5.0)[23] were freshly prepared in 50 mM Tris–HCl pH 8.0, and 150 mM NaCl. $K_3Fe(CN)_6$ and $K_4Fe(CN)_6$ spectra were independently acquired to assign the individual $\nu(C\equiv N)$ stretching modes (Fig. S1‡).

Electron paramagnetic resonance spectroscopy. The HoxC and RH samples were analyzed in a concentration range of 0.5–1.0 mM and 0.1–0.3 mM (70–100 μL), respectively. HoxC and RH

protein solutions were transferred into 4 mm quartz EPR tubes, quenched in cold ethanol (193 K) and frozen in liquid nitrogen for further analysis. A Bruker EMXplus spectrometer equipped with an ER 4122 SHQE resonator, an Oxford EPR 900 helium flow cryostat and an Oxford ITC4 temperature controller was used for EPR measurements. The baseline correction of the experimental spectra was done by subtracting the spectrum of the buffer solution measured with the same parameters. If necessary, the spectra were additionally corrected by using a polynomial or spline function. Experimental parameters: 1 mW microwave power, microwave frequency 9.29 GHz, modulation amplitude 10 G and 100 kHz modulation frequency. Spectral simulation was performed with Matlab toolbox Easyspin 5.2.25.

Mössbauer. Zero-field Mössbauer spectra were recorded on a SEECO MS6 spectrometer that comprises the following instruments: a JANIS CCS-850 cryostat, including a CTI-CRYOGENICS closed cycle 10 K refrigerator, and a CTI-CRYOGENICS 8200 helium compressor. The cold head and sample mount were equipped with calibrated DT-670-Cu-1.4L silicon diode temperature probes and heaters. Temperature was controlled by using a LAKESHORE 335 temperature controller. Spectra were recorded using a LND-45431 Kr gas proportional counter with a beryllium window connected to a SEECO W204 γ-ray spectrometer that included a high voltage supply, a 10 bit and 5 μs ADC and two single channel analyzers. Motor control and recording of the spectra were taken care of by using a W304 resonant γ-ray spectrometer. For the reported spectra a RIV-ERTEC MCO7.114 source (^{57}Co in Rh matrix) with an activity of about 1 GBq was used. All the spectra were recorded on frozen solutions at 13 K and data were accumulated for about 24 hours. Mössbauer data were processed and simulated using the WMOSS4 program (https://www.wmoss.org). Isomeric shifts were referenced to α-iron at room temperature. [^{57}Fe]-HoxC and [^{57}Fe]-HoxC$_{ox}$ were analyzed in a concentration range of 1–1.5 mM.

Time-dependent density functional theory (TDDFT) calculations. The active site models used for the TDDFT calculations included Ni and Fe atoms and their first coordination spheres and their initial geometries were based on the [NiFe]-hydrogenase active site of *Desulfovibrio fructosovorans* (pdb code: 1YRQ).[24] The four metal-coordinating cysteine residues were truncated at the level of their C_β atoms, whose coordination sphere was subsequently saturated by adding an H atom. Calculations on the resulting models were carried out using the CAM-B3LYP exchange–correlation functional.[25] A def2-TZVP basis set[26] was used for all the atoms to carry out geometry optimization, which was followed by the UV-vis spectral prediction, as detailed below. All calculations were carried out with GAUSSIAN16 software,[27] upon constraining the cysteine C_β atoms at their crystallographic positions. If not otherwise stated, the cysteine C_β atoms were the only geometric constraints imposed on the models. The models were soaked in the polarizable continuum model PCM[28,29] implemented in GAUSSIAN16. We chose a dielectric constant of $\varepsilon = 4$, which was shown to be appropriate for metalloprotein modeling,[30–32] and the remaining PCM parameters were maintained at their

default values.[27] For our models, we considered both water-ligated and hydroxo-ligated species, which had an overall charge of −2 and −3e, respectively. Self-consistent field computations were carried out within the closed-shell framework. Indeed, efforts to localize broken-symmetry open-shell singlets[33] led to convergence on non-spin-polarized solutions. As far as the computation of UV-vis theoretical spectra is concerned, TDDFT calculations were performed using the optimized geometries and the corresponding electronic structures. Altogether 20 states were considered for TDDFT computations for each of the optimized structures.

Results

HoxC contains an integral NiFe(CO)(CN)$_2$ cofactor

As-isolated HoxC protein (HoxC$_{ai}$) was overproduced in *R. eutropha* and subsequently purified by affinity chromatography as described in the Experimental section and the ESI (Fig. S2 and S3‡). ICP-OES measurements of the purified HoxC$_{ai}$ samples revealed the presence of (1.10 ± 0.05) Fe and (1.06 ± 0.03) Ni (Fe/Ni = 0.96), indicating full occupancy by the [NiFe] cofactor. The pale brownish color of the protein samples tempted us to perform UV-vis absorption spectroscopy. Indeed, a diluted HoxC$_{ai}$ sample (15 μM) displayed a weak absorption in the region between 360 nm and 400 nm, while a more concentrated sample (200 μM) showed even two maxima at 370 nm and 390 nm (Fig. 2A). Based on the protein concentration, we calculated an apparent molar extinction coefficient of $\varepsilon =$ (3800 ± 400) M^{-1} cm^{-1}. We assigned this particular UV-vis absorption to the NiFe(CO)(CN)$_2$ cofactor, which was thus far undetectable due to the superimposed absorption of the FeS clusters present in the hydrogenase small subunit.

Further evidence for the correct incorporation of the [NiFe] cofactor into HoxC$_{ai}$ was obtained by IR spectroscopy, which probed the ν(C≡O) (1870–2020 cm^{-1}) and ν(C≡N) (2030–2150 cm^{-1}) stretching modes of the CO and CN$^-$ ligands of the [NiFe] catalytic center.[4,34] After aerobic purification, the IR spectrum of HoxC$_{ai}$ exhibited two CO bands at 1941 cm^{-1} and 1952 cm^{-1} and two broad CN-related absorptions at 2066 cm^{-1} and 2084 cm^{-1}. The IR spectrum of as-isolated RH, for comparison, showed frequencies at 1943 cm^{-1}, 2070 cm^{-1}, and 2081 cm^{-1}, attributed to the Ni$_a$-S state of the active site (Fig. 1, 2B and Table S1‡).[13,35]

Thus, metal content determination, and UV-vis, and IR spectroscopy confirmed that HoxC is completely loaded with an intact NiFe(CO)(CN)$_2$ cofactor. The IR band broadening, however, indicated certain structural heterogeneity of the active site in HoxC$_{ai}$ when compared to that in RH. In fact, the presence of two CO vibrations suggests different conformations or/and redox states of the [NiFe] active site. To get a clue about the origin of these different conformations, we checked first the integrity of isolated HoxC$_{ai}$ by size-exclusion chromatography (Fig. S3‡). Indeed, HoxC$_{ai}$ occurred in a monomeric and a dimeric version. Both versions were subjected to IR spectroscopy which revealed identical spectra (Fig. S4‡). Thus, the two different CO vibrations were not a result of the mixture of monomeric and dimeric HoxC$_{ai}$, and all further experiments were therefore performed with HoxC$_{ai}$ protein obtained after

affinity chromatography. Remarkably, extended exposure of HoxC$_{ai}$ to carbon monoxide, hydrogen gas or even sodium dithionite (4-fold molar excess) revealed no significant changes of the original IR spectrum (Fig. S5‡). Thus, HoxC$_{ai}$ does not apparently bind exogenous CO and withstands reduction at physiological redox potentials.

To investigate whether the two HoxC$_{ai}$ active site states related to the CO stretching modes at 1941 cm^{-1} and 1952 cm^{-1} represent different protonation states of the "same" redox species, we carried out pH dependent IR spectroscopic measurements (Fig. 2C). HoxC$_{ai}$, which was initially purified at pH 8.0, was equilibrated with buffer at pH 6.0. This pH shift resulted in an increase of the stretching band at 1941 cm^{-1}, while the absorption at 1952 cm^{-1} dropped in intensity (Fig. 2C, traces a and b). The process turned out to be reversible, as the return to pH 8.0 revealed the initial ratio of the bands at 1952 cm^{-1} and 1941 cm^{-1} (Fig. 2C, trace e). As the HoxC$_{ai}$ protein was unstable at pH values lower than 5.5 and higher than 9.0, it was impossible to isolate the [NiFe] site in only one of the two states. However, by obtaining difference spectra (pH 8.0–6.0), we were able to deconvolute the CO/CN bands and delineate the two individual states in almost pure forms (Fig. 2C, traces c and d). Based on the results of the pH-dependent IR analysis of HoxC$_{ai}$ and the apparent lack of reactivity of the protein towards exogenous H$_2$ and CO gases (Fig. S5‡), we attributed the two CO modes to the two isoelectronic Ni$_r$-S$_I$ and Ni$_r$-S$_{II}$ states, which just differ in their degree of protonation. Taking into account previous observations for standard [NiFe]-hydrogenases,[36–38] the main CO band at 1952 cm^{-1} was assigned to Ni$_r$-S$_I$, which supposedly contained a metal-bridging hydroxo ligand resulting in a Ni^{II}-(OH$^-$)-Fe^{II}(CO)(CN)$_2$ configuration of the active site. By lowering the pH, the bridging hydroxo ligand became protonated, thereby yielding a bound H$_2$O molecule,[37,39] which resulted in the Ni$_r$-S$_{II}$ state with a Ni^{II}-(HOH)-Fe^{II}(CO)(CN)$_2$ structure and a ν(C≡O) stretching vibration at 1941 cm^{-1}.

While the IR spectroscopic measurements allowed the pH-dependent separation of the Ni$_r$-S$_I$ and Ni$_r$-S$_{II}$ species in HoxC$_{ai}$, the corresponding UV-visible spectrum was recorded exclusively at pH 8.0 (Fig. 2A), because the two absorption maxima at 370 and 390 nm were not sufficiently separated to expect pH-dependent variations. However, the presence of the two inter-convertible water-based active site species in the HoxC$_{ai}$ preparation prompted us to investigate whether the UV-vis spectrum absorptions shown in Fig. 2A can be reproduced by time-dependent density functional theory (TDDFT) calculations based on geometry-optimized [NiFe] cofactor models. Indeed, the characteristic absorption maxima below 300 nm and 370 and 390 nm were mimicked only by assuming the co-presence of Ni^{II}-(HOH)-Fe^{II} and Ni^{II}-(OH)-Fe^{II} species, both of them carrying low-spin metal centers (see ESI, Fig. S6–S9 and Tables S2–S4‡).

In contrast to HoxC$_{ai}$, as-isolated RH resided predominantly in the Ni$_a$-S state at pH values ranging between 5.5 and 9.0 (Fig. S10A‡). Interestingly, the IR spectrum also contained a minor ν(C≡O) stretching mode at 1963 cm^{-1}, which was most enriched at pH 5.5 (Fig. S10A‡). Upon further exposure to O$_2$ (at pH 5.5), which was accomplished by slow air diffusion into the
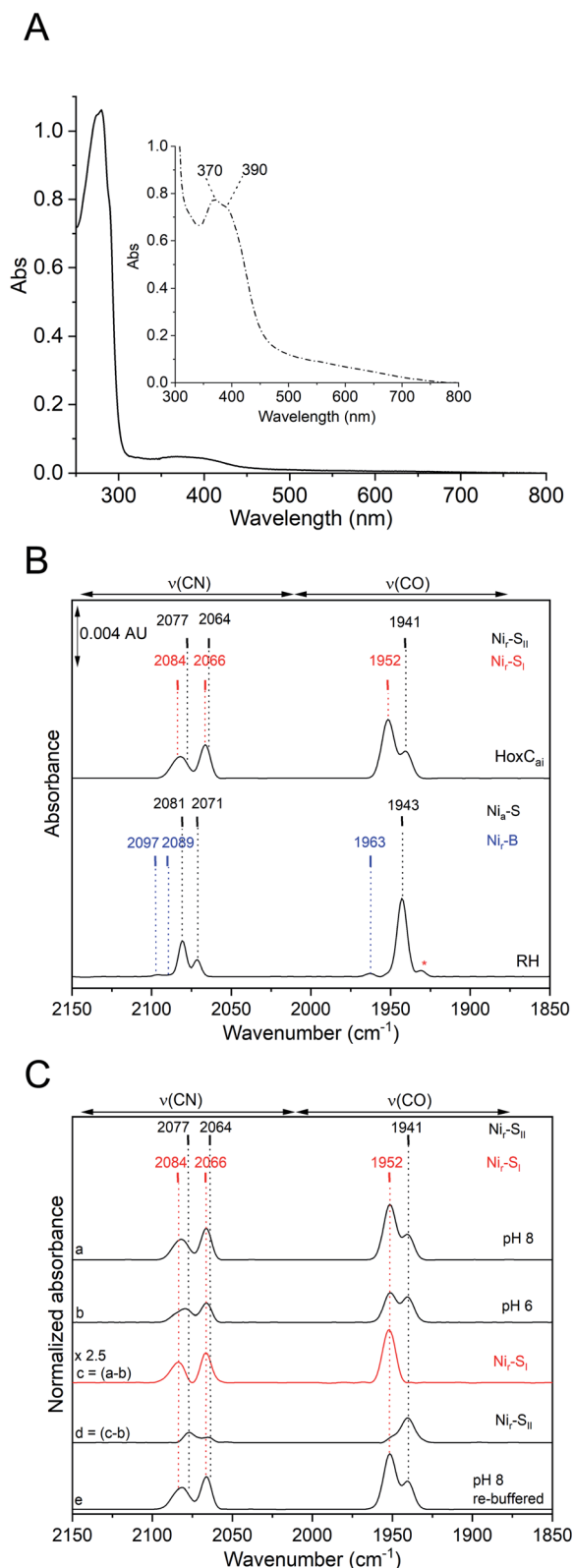
A

B

C

Fig. 2 Spectroscopic characterization of HoxC$_{ai}$. (A) UV-vis absorption spectra of diluted (solid line) and concentrated (inset, dash-dotted line) HoxC$_{ai}$ showing two bands at 370 and 390 nm. (B) Comparison of the IR absorbance spectra of HoxC$_{ai}$ (top) and as-isolated RH (bottom) at a concentration of 0.2 mM and pH 8.0. (C) IR absorbance spectra of HoxC$_{ai}$ recorded at pH 8.0 (trace a) and pH 6.0 (trace b) were normalized to the intensity at 1941 cm^{-1}. Trace c (magnified by a factor

transmission cell, the band at 1963 cm^{-1} increased further, and $\nu(C\equiv N)$ stretching vibrations at 2089 and 2097 cm^{-1} became clearly visible (Fig. S10B‡). The CO-related band at 1963 cm^{-1} has already been assigned to the Ni$_r$-B state of RH, while the corresponding $\nu(C\equiv N)$ stretching modes were not resolved in the previous study.[12]

The [NiFe] cofactor of HoxC responds to chemical oxidation

The IR spectrum of HoxC$_{ai}$ did not show any detectable changes when the protein was incubated with either H$_2$ or CO (Fig. S5‡). Treatment with two different chemical oxidants, K$_3$Fe(CN)$_6$ and K$_2$Ir(Cl)$_6$, however, resulted in distinct frequency upshifts of the CO- and CN-related bands (Fig. 3A, S11A and B‡), indicating oxidation of the [NiFe] cofactor. The IR spectrum of K$_3$Fe(CN)$_6$-oxidized HoxC (HoxC$_{ox}$) revealed a broadened CO absorption at 1978 cm^{-1} with a shoulder at 1969 cm^{-1}. CN ligand-related signals were observed at 2081 and 2090 cm^{-1} (Fig. 3A and Table S1‡). The prominent band at 2116 cm^{-1} corresponds to the $\nu(C\equiv N)$ stretching of Fe(CN)$_6^{3-}$, while the peak at 2036 cm^{-1} belongs to the $\nu(C\equiv N)$ stretching of the 1e$^-$ electron reduced Fe(CN)$_6^{2-}$ (Fig. S1‡). A very similar spectrum was obtained upon incubation of HoxC$_{ai}$ with the stronger oxidant K$_2$Ir(Cl)$_6$ (Fig. 3A). While 2–3 equivalents of K$_3$Fe(CN)$_6$ were sufficient to oxidize HoxC completely, 25 equivalents of K$_2$Ir(Cl)$_6$ were required to obtain the quantitatively oxidized [NiFe] cofactor. The higher demand for the iridium compound can be explained by its redox potential of +0.96 V, which is large enough to extract electrons from H$_2$O.[40] Nonetheless, since the treatments with K$_2$Ir(Cl)$_6$ and K$_3$Fe(CN)$_6$ resulted in exactly the same HoxC-derived IR bands, we can exclude that further $\nu(C\equiv O)$ or $\nu(C\equiv N)$ stretching modes were covered by the contribution of Fe(CN)$_6^{2-}$/Fe(CN)$_6^{3-}$ modes (Fig. 3A, S11A, B and S1‡). As for HoxC$_{ai}$, treatment of RH enzyme with K$_3$Fe(CN)$_6$ led to the formation of Ni$_r$-B, but only in minuscule amounts (Fig. S12A‡).

The blue shift of the $\nu(C\equiv O)$ stretching modes upon oxidation (Fig. 3A) indicated a change in the redox state of the catalytic center of HoxC$_{ai}$. In the case of [NiFe]-hydrogenases, nickel has been identified to play the key role as it can adopt the diamagnetic 2+ state and the paramagnetic 1+ and 3+ states (Fig. 1).[4,41] Therefore, we investigated the different redox states of HoxC by EPR spectroscopy (Fig. 3B). HoxC$_{ai}$ appeared to be EPR silent, which is in accordance with the low-spin Ni^{II}–Fe^{II} configuration of the active site present in the diamagnetic Ni$_r$-S$_I$ and Ni$_r$-S$_{II}$ states. The EPR spectrum of HoxC$_{ox}$ displayed a rather rhombic signal (Fig. 3B blue trace and S11C‡). By using numerical simulation, the complexity of the spectrum was deconvoluted and interpreted with at least two different overlapping rhombic signals of paramagnetic ($S = 1/2$) Ni^{III} species (Fig. S11D‡). Further EPR measurements at varying microwave

---

2.5 to match the intensity in a) displays the difference spectrum of "a" minus "b" to isolate the active site state prevailing at high pH. In the difference spectrum d, trace b is subtracted from trace c to isolate the species dominating at low pH. Trace e represents the spectrum of HoxC$_{ai}$, first incubated at pH 6.0 and subsequently buffered at pH 8.0, which demonstrates the interconvertibility of the active site states.
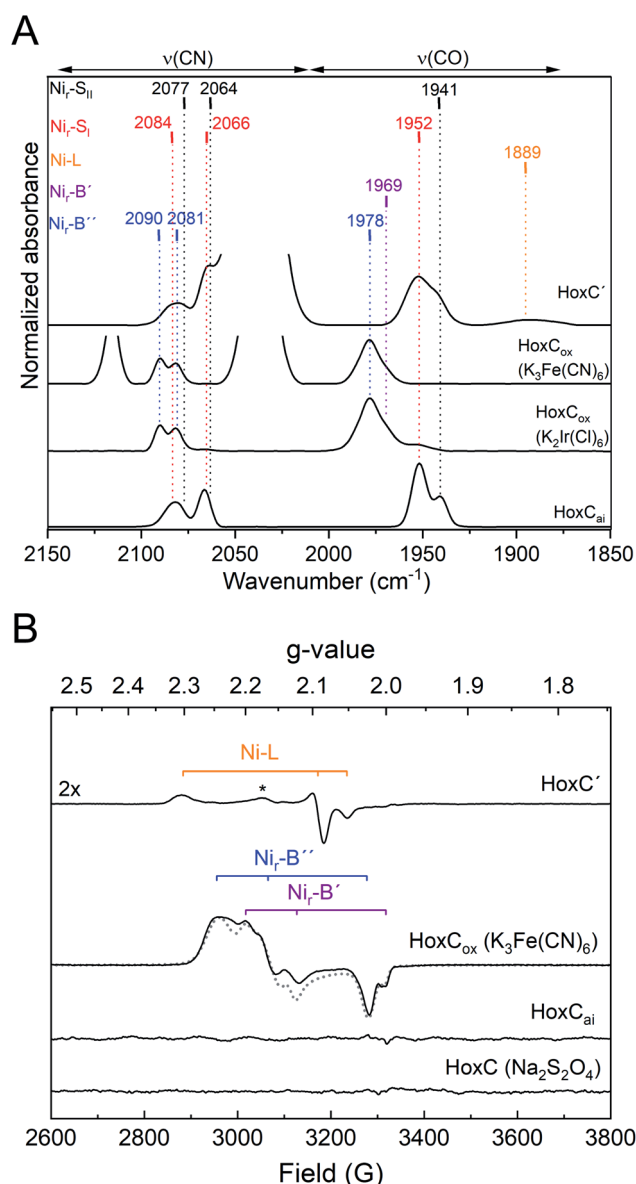
A

B

Fig. 3 IR and EPR spectroscopic characterization of HoxC preparations treated with chemical oxidants and reductants. (A) IR absorbance spectra (normalized to the protein concentration) of redox-treated HoxC preparations. From bottom to top: $HoxC_{ai}$, $HoxC_{ox1}$ ($HoxC_{ai}$ oxidized with 28 equivalents of $K_2Ir(Cl)_6$), $HoxC_{ox2}$ ($HoxC_{ai}$ oxidized with 4 equivalents of $K_3Fe(CN)_6$), and HoxC′ (prepared from $K_3Fe(CN)_6$-oxidized $HoxC_{ox}$ and subsequently reduced with $Na_2S_2O_4$). Color-coded (redox) states: red, Ni_r-S_I; black, Ni_r-S_{II}; orange, Ni-L; magenta, Ni_r-B′; and blue, Ni_r-B″. Absorptions of $[Fe(CN)_6]^{3-}$ (2116 cm^{-1}) and $[Fe(CN)_6]^{2-}$ (2036 cm^{-1}) were partially cut to emphasize the bands related to vibrational modes of the active site. (B) EPR spectra of redox-treated HoxC preparations measured at 20 K. From bottom to top: HoxC ($HoxC_{ai}$ treated with sodium dithionite), $HoxC_{ai}$, $HoxC_{ox}$ ($HoxC_{ai}$ oxidized with 2 equivalents of $K_3Fe(CN)_6$, and HoxC′ (prepared from $K_3Fe(CN)_6$-oxidized $HoxC_{ox}$ and subsequently reduced with $Na_2S_2O_4$). The asterisk in the HoxC′ spectrum denotes the signal of a so far unknown paramagnetic Ni species. The simulated spectrum of $HoxC_{ox}$ including the signals for Ni_r-B′ and Ni_r-B″ species is shown as a dotted line. The simulations of the single EPR spectra are shown in Fig. S11D.‡

power and different temperatures revealed a very similar spin relaxation behavior and, hence, indicated a structural and electronic similarity of the two species (Fig. S13‡). Based on the observed characteristic blue shift in the IR spectra upon oxidation, the presence of paramagnetic Ni^{III}, and the reducibility of the state(s) (see below), we infer a Ni^{III}-(OH$^-$)-Fe^{II}(CO)(CN)$_2$ configuration in $HoxC_{ox}$. In classical heterodimeric [NiFe]-hydrogenases this active site configuration is designated as Ni_r-B (Fig. 1).[42,43] Based on the relative intensities of the CO vibrations at 1969 and 1978 cm^{-1} (Fig. S11B‡) and the corresponding intensities of the simulated EPR spectra (Fig. S11D‡), we assign these frequencies to Ni_r-B′ and Ni_r-B″, respectively (Table S5‡). Notably, accurate simulation of the Ni_r-B″-related EPR spectrum required the implementation of an unusually large g-strain. This indicates structural heterogeneity, which is probably caused by an enhanced flexibility of the [NiFe] cofactor. Such flexibility would also explain the large band broadening observed for the ν(C≡O) stretching mode at 1978 cm^{-1} (Fig. 3A, S11A and B‡). It is worth noting that a small paramagnetic signal indicative of Ni_r-B was also observed for the RH protein (Fig. S12B‡), which correlates with the IR-based ν(C≡O) stretching mode at 1963 cm^{-1} (Fig. S10‡).[12]

To identify the redox and spin state(s) of the active site iron, we performed Mössbauer spectroscopy on ^{57}Fe-labelled HoxC protein. In fact, the isolated HoxC subunit allowed for the first time an unadulterated view of the single iron in the catalytic center, which is usually masked by the numerous iron atoms of the FeS clusters in standard hydrogenase preparations containing the small subunit. Mössbauer spectroscopy showed that the active site iron ion in $HoxC_{ai}$ is characterized by a low isomer shift ($\delta = 0.14$ mm s^{-1}), which hardly differs from $HoxC_{ox}$ ($\delta = 0.15$ mm s^{-1}) (Fig. 4 and S14‡). The additional low-intensity resonances are derived from high-spin Fe^{II} contamination with a 8–10% partitioning. Also the quadrupole splitting parameters of the iron ions in HoxC ($\Delta E_Q = 0.65$ mm s^{-1}) and $HoxC_{ox}$ ($\Delta E_Q = 0.59$ mm s^{-1}) are comparable (Table S6‡), reflecting a similar electric field and, thus, a comparable ligand environment in both states. These observations are in agreement with the active site iron(II) ion persisting in the low-spin state, which is consistent with the current view on the catalytic properties of the [NiFe] cofactor.[4]

The oxidized [NiFe] cofactor of HoxC responds to chemical reduction

As described above, $HoxC_{ai}$ protein turned out to be inert to reductants (Fig. S5‡). Therefore, we tested whether $K_3Fe(CN)_6$-oxidized $HoxC_{ox}$ can be reduced. Indeed, upon addition of sodium dithionite, the CO- and CN-related bands shifted back to their original positions as previously observed for $HoxC_{ai}$ (Fig. 3A). Only a minor change in the ratio of the Ni_r-S_I and Ni_r-S_{II} states was observed. Because of the almost identical IR pattern compared to $HoxC_{ai}$, we denoted dithionite-treated $HoxC_{ox}$ as HoxC′. Notably, a minor broad band appeared at 1889 cm^{-1} upon reductive treatment (Fig. 3A). CO stretching vibrations in this spectral region are commonly related to the Ni-L state, characterized by a Ni^I-(–)-Fe^{II}(CO)(CN)$_2$ configuration of
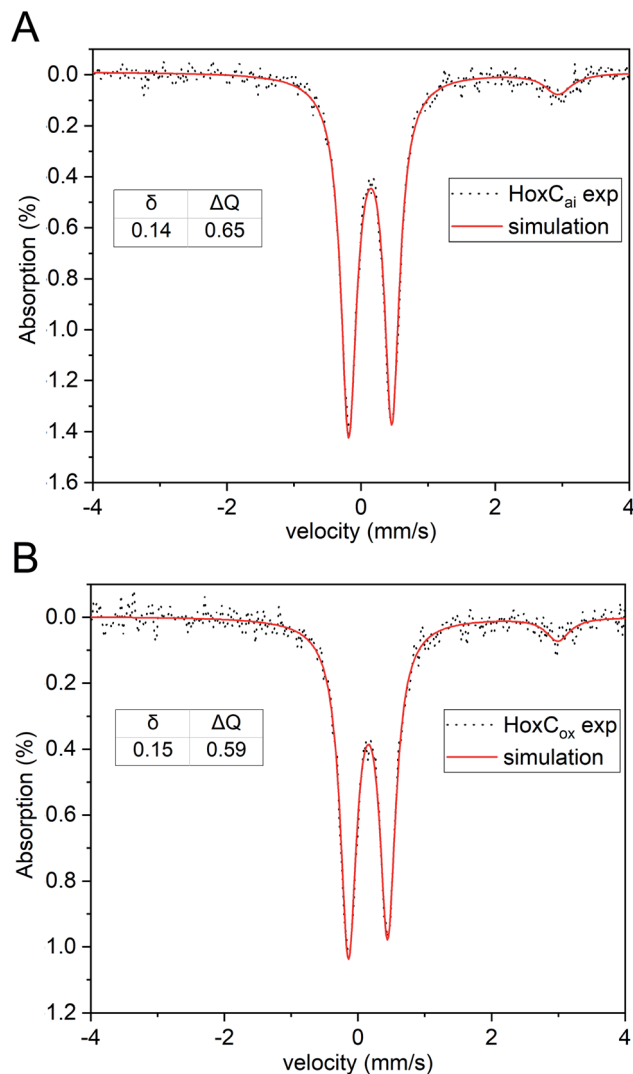
Fig. 4 Mössbauer spectra of ^{57}Fe-labelled HoxC in the as-isolated form (A) and chemically oxidized with $K_3Fe(CN)_6$ (B). Black dots represent the experimental data. Red lines indicate the simulations, and the corresponding isomer shifts (δ) and quadrupole splittings (ΔE_Q) are shown. Low-intensity signals of high-spin Fe^{II} were also detected (δ = 1.43, ΔE_Q = 3.02 mm s^{-1} for HoxC$_{ai}$ and δ = 1.43, and ΔE_Q = 3.13 mm s^{-1} for HoxC$_{ox}$) representing 8–10% of the total iron content.

the active site.[4,44] EPR spectroscopy confirmed the presence of a paramagnetic species in HoxC′ resembling the spectral signature of Ni-L (Fig. 3B and Table S5‡). In accordance with the IR data, however, the Ni-L state occurred only in traces (Fig. 3A).

H$_2$ splitting capacity of HoxC

[NiFe]-hydrogenases are known to perform the catalytic hydrogen/deuterium (H/D) exchange reaction,[5,45,46] which is independent of long-range electron transfer mediated by the iron–sulfur clusters in the small subunit. Therefore, it is particularly suited for probing the H$_2$ binding and splitting capacity of isolated large subunits.[5] The catalytic H/D exchange reaction occurs according to the reactions:

$$H_2 + D_2O \rightleftharpoons HD + HDO \qquad (1)$$

$$HD + D_2O \rightleftharpoons D_2 + HDO \qquad (2)$$

Thus, the reversible H$_2$ splitting capacity of a given catalyst can be derived by measuring H$_2$ consumption and the concomitant production of HD and D$_2$. The HoxC samples were placed in D$_2$O-based buffer and the reaction was started by addition of H$_2$-saturated buffer. The release of gaseous products was measured with a mass spectrometer by monitoring the mass-to-charge ratios (m/z) 3 and 4, indicative of HD and D$_2$, respectively (Fig. 5A). Purified HoxC showed highest activities at pH 4.5, with HD and D$_2$ production rates of 0.89×10^{-3} s^{-1} and 0.19×10^{-3} s^{-1}, respectively (HD/D$_2$ = 4.5, Table S7‡). To verify the significance of these low activities, we conducted control experiments with bovine serum albumin and a hydrogenase maturase complex, consisting of HypCD proteins carrying the Fe(CO)(CN)$_2$ unit of the [NiFe] cofactor.[47] Both samples did not show any catalytic H/D exchange activity (Fig. S15‡). Furthermore, the HD and D$_2$ evolution rates of purified HoxC increased linearly dependent on both the protein (Fig. S16‡) and H$_2$ concentration (Fig. S17‡). Notably, no differences in activity and the HD/D$_2$ ratios were detected for the monomeric and dimeric forms of HoxC (Fig. S18‡). The HoxC-mediated H/D exchange activity decreased at pH values < 4.0, which was likely caused by protein instability. At pH values above 7.0, HD and D$_2$ production was not detected anymore. A comparative investigation was performed with the RH protein, revealing the highest HD and D$_2$ production rates of 460×10^{-3} s^{-1} and 1802×10^{-3} s^{-1}, respectively, at pH 7.0 (Fig. S19 and Table S7‡). At pH 5.0 the HD production of RH was 235×10^{-3} s^{-1}, *i.e.* more than 200-fold higher than that of HoxC (Fig. S19‡ and 5A). RH-mediated activity was observed at pH 3 up to pH 9, which correlates with the prevailing Ni$_a$-S species in as-isolated RH within a broad pH interval (Fig. S10A‡).

Next, we investigated whether HoxC is able to split H$_2$ reversibly also in the presence of O$_2$. In a previous study, we showed that the catalytic H/D exchange performed using the purified premature MBH large subunit, preHoxG, is only barely affected by O$_2$, even if added at a high concentration.[5] Native RH has also been shown to sustain catalytic activity in the presence of O$_2$.[48] We measured the catalytic H/D exchange activity of HoxC at pH 4.5 in the presence of 5, 10, and 20% (v/v) O$_2$-saturated buffer while keeping the initial H$_2$ concentration (Fig. 5B) constant. When compared to O$_2$-free reaction conditions, HoxC maintained 84.5% of HD and 58% of D$_2$ production rates at 20% O$_2$. Notably, the HD production activity was less affected by O$_2$ than the D$_2$ production (Fig. 5B). This can be easily explained by the longer exposure of the catalytic center to O$_2$ in the case of the complete conversion of H$_2$ into D$_2$ *via* HD.

We also tested the capability of HoxC to transfer electrons derived from H$_2$ oxidation to an artificial electron acceptor. Indeed, HoxC catalyzed the H$_2$-mediated reduction of methylene blue, a two-electron acceptor with $E^{0\prime}$ = +40 mV, with a specific activity of (0.010 ± 0.001) U mg^{-1} at pH 5.2 (Fig. S20‡). It is, however, unclear whether the electrons are transferred to the dye in a step-wise mechanism or even as a hydride. No
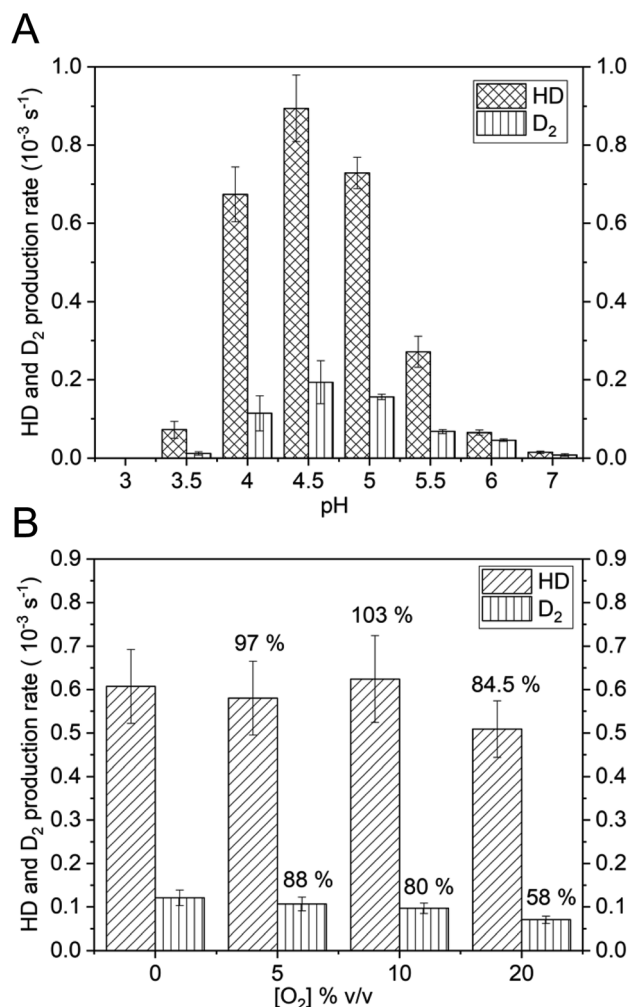
Fig. 5 HoxC-mediated H_2 activation. (A) HD and D_2 production rates of $HoxC_{ai}$ as a function of the pH. 100–200 μg of $HoxC_{ai}$ were incubated with H_2 gas in a D_2O-based buffer at different pH values. (B) HD and D_2 production rates of $HoxC_{ai}$ (pH 4.5) in the presence of different O_2 concentrations. The values provided at the top of the columns denote the rates in relation to the rate determined in the absence of O_2. Error bars indicate the standard deviation calculated from three independent measurements.

activity was determined in the absence H_2 (replaced by N_2) or without the protein. Moreover, the activity significantly decreased at pH values lower than 4.0 and higher than 5.5, which is consistent with the pH dependency of the catalytic H/D exchange reaction (Fig. 5A). Purified RH protein, for comparison, catalyzes H_2 oxidation with a specific activity of (3.8 ± 0.5) U mg^{-1} at pH 7.0. At pH 5.2, RH activity decreases to 2.0 ± 0.1 U mg^{-1}, which is still more than 200-fold higher than that of HoxC (Fig. S20‡).

Discussion

In this study we investigated an isolated, fully assembled large subunit of a [NiFe]-hydrogenase by means of biochemical and spectroscopic methods. Isolated [NiFe]-hydrogenase large

subunits have been analyzed before, but they were either sub-stoichiometrically loaded with nickel[5,18] or even did not contain metal ions at all.[6] The stoichiometric presence of both nickel and iron in HoxC allowed for the first time determination of the UV-visible molar extinction coefficient of the [NiFe] cofactor with $\varepsilon = 3800$ M^{-1} cm^{-1}. This value is much lower than that of [4Fe–4S] clusters[49] (13 000–16 000 M^{-1} cm^{-1}) which generally dominate the electronic absorbance properties of [NiFe]-hydrogenases. Due to the lack of more appropriate *in vitro*/*in silico* model systems, we compared the HoxC spectroscopic signatures to those of bioinspired [NiFe] model compounds carrying low-spin ($S = 0$) Ni^{II} and Fe^{II} ions.[50–52] Moreover, the UV-vis spectrum of $HoxC_{ai}$ could be well-reproduced by TDDFT calculations on active site models carrying low-spin Ni^{II} and Fe^{II} centers that are occupied by water derived ligands, which perfectly agrees with the corresponding biochemical and spectroscopic data (see below).

The presence of an intact $[NiFe(CO)(CN)_2]$ cofactor was verified by IR spectroscopy. However, in contrast to RH (HoxBC), which occurs almost completely in the catalytically competent Ni_a-S state (Ni^{II}-(–)-$Fe^{II}(CO)(CN)_2$)[10] (Fig. 2), $HoxC_{ai}$ resides predominantly in the Ni_r-S conformation (Ni^{II}-(OH^-)-$Fe^{II}(CO)(CN)_2$). The absence of EPR-detectable signals for $HoxC_{ai}$ further supports a diamagnetic low-spin Ni^{II}–Fe^{II} arrangement of the active site, as is also suggested to be present in standard [NiFe]-hydrogenases.[10,14,53] Thus, despite aerobic purification, active site nickel remained in the 2+ state, while the iron center retained a low-spin Fe^{II} configuration. The latter was verified by Mössbauer spectroscopy of ^{57}Fe-labelled HoxC protein (Fig. 4). So far, Mössbauer studies on [NiFe]-hydrogenases (^{13,54}) including RH have revealed spectra that were dominated by iron–sulfur cluster signals from the three [4Fe–4S] clusters, which required sophisticated simulation procedures to deconvolute the contributions of single Fe species. In the case of RH, for instance, the signal of active site iron contributed only 7% to the total spectrum (Table S6‡).[13] Nevertheless, the isomer shift and quadrupole splitting of the iron atom of the RH active site in the Ni_a-S state have been calculated to be 0.1 mm s^{-1} and 1.60 mm s^{-1}, respectively. In reduced RH, which resides predominantly in the in Ni_a-C state, however, the isomer shift and quadrupole splitting shifted to 0.07 mm s^{-1} and 0.69 mm s^{-1}, respectively, suggesting significant changes in the ligand environment of the Fe^{II} ion upon reduction. In fact, the observed decrease in the quadrupole splitting has been correlated with the change from 5-fold coordinated Fe^{II} in the Ni_a-S state $[Ni^{II}$-(–)-$Fe^{II}(CO)(CN)_2]$ to 6-fold coordinated Fe^{II} in Ni_a-C $[Ni^{III}$-(H^-)-$Fe^{II}(CO)(CN)_2]$.[13] Our Mössbauer investigations on ^{57}Fe-labelled HoxC allowed an exclusive view of the corresponding signal of the low-spin Fe^{II} in the active site (Fig. 4 and S14‡). Interestingly, the quadrupole splitting parameters for $HoxC_{ai}$ and $HoxC_{ox}$ are similar (0.65 *vs.* 0.59 mm s^{-1}) to each other and both are close to that of the Ni_a-C state of RH (0.69 mm s^{-1}).[13] This suggests that the number of iron ligands did not vary among the three species, but only the oxidation state of nickel varied. This observation is supportive of a 6-fold coordination of the iron

atoms of both HoxC$_{ai}$ and HoxC$_{ox}$, in line with the proposed presence of bridging H$_2$O or OH$^-$ ligands of the active site in the Ni$_r$-S and Ni$_r$-B states.

According to our EPR measurements, the [NiFe] site changed from a diamagnetic state in HoxC$_{ai}$ into a paramagnetic state in HoxC$_{ox}$ (Fig. 3B). The corresponding spectrum, however, contains two different species whose spectral signatures deviate from that of the standard Ni$_r$-B state (Fig. S11D‡). Hence, we denote these so far unknown states as Ni$_r$-B' and Ni$_r$-B'' (see Table S5‡ for g-values). The occurrence of the two states instead of a pure Ni$_r$-B spectrum supports different arrangements of the [NiFe] core, as a result of an increased conformational flexibility of HoxC lacking the small subunit HoxB. The increased conformational flexibility compared to that of the native enzyme might also explain the relatively high frequency of the CO modes of the Ni$_r$-B''' species (Fig. 3A). Chemical reduction of HoxC$_{ox}$ with dithionite resulted in a minor appearance of Ni-L species (Ni^I-(–)-Fe^{II}(CO)(CN)$_2$), which is nowadays discussed to be an intermediate of the catalytic cycle.[16,55] In the present case, Ni-L seems to be derived from the paramagnetic Ni$_r$-B'–Ni$_r$-B'' species under 2e$^-$ reduction provided by the dithionite treatment (reductant) involving water and/or OH$^-$ release and remains kinetically trapped. However, most of the dithionite-reduced HoxC$_{ox}$ population remained diamagnetic and was dominated by Ni$_r$-S$_I$ and Ni$_r$-S$_{II}$ species (Fig. 3).

Our data show that HoxC is redox-active and occurs in active site resting states common to [NiFe]-hydrogenases. However, apart from minor amounts of Ni-L, no states related to the catalytic cycle (Fig. 1A) were enriched. In fact, some of the intermediates observed for HoxC, including all Ni$_r$-S states, are essentially absent in fully assembled RH. Although the isolated HoxC and the HoxC subunits in RH share the same amino acid composition, the absence of the small subunit obviously changes the environment of the active site in a way that prevents canonical H$_2$/H$^+$ cycling. Nevertheless, HoxC is capable of activating molecular hydrogen, as has been previously observed for the isolated large subunit, preHoxG, of the membrane bound hydrogenase of *R. eutropha*.[5] The catalytic H/D exchange activity of the two proteins in D$_2$O-based buffer is based on their capacity to split H$_2$ into H$^+$ and H$^-$, resulting in the detectable products HD and D$_2$. The HD/D$_2$ production rates were 0.89 × 10^{-3}/0.193 × 10^{-3} s^{-1} for HoxC and 0.74 × 10^{-3}/2.04 × 10^{-3} s^{-1} for preHoxG.[5] The RH and MBH of *R. eutropha*, by contrast, showed HD and D$_2$ production rates of 460 × 10^{-3} s^{-1}/1802 × 10^{-3} s^{-1} and 11.21 × 10^{-3} s^{-1}/12.55 × 10^{-3} s^{-1}, respectively (Table S7‡).[5] Thus, HoxC has a considerably lower activity than RH but the HD production rate of RH is only 12 times lower compared to that of MBH. Besides, HoxC activity was linearly dependent on the amount of the enzyme and substrate (Fig. S16 and S17‡). We conclude that the absence of the confining and hydrophobic environment created by the small subunit decreased the affinity for H$_2$. Consistently, only small variations in the HD/D$_2$ ratios were observed for different HoxC concentrations (Table S8‡), which indicates the absence of a prominent cage effect. By contrast, the corresponding HD/D$_2$ ratios of native [NiFe]-hydrogenases were shown to be highly dependent on the enzyme concentration.[46,56]

Notably, the highest HoxC activity was observed under rather acidic conditions, and only negligible activity was measured at physiological pH. This is consistent with our IR data that show that the Ni$_r$-S$_I$ state (Ni^{II}-(OH$^-$)-Fe^{II}(CO)(CN)$_2$) dominates at high pH. Upon lowering the pH, the bridging hydroxo ligand becomes protonated resulting in the formation of the Ni$_r$-S$_{II}$ species (Ni^{II}-(HOH)-Fe^{II}(CO)(CN)$_2$). An acid–base equilibrium has also been described for the Ni-S states of standard [NiFe]-hydrogenases,[39,57–59] where accumulation of the Ni$_a$-S state was observed as a result of protonation of the bridging OH$^-$ ligand of the Ni$_r$-S state. The corresponding H$_2$O molecule might be located in proximity of the active site. In the case of HoxC$_{ai}$, with a rather solvent-exposed catalytic cofactor, however, water may remain in the bridging position of the active site. Only a small HoxC fraction in the Ni$_r$-S$_{II}$ state lost the bridging water ligand, resulting in the formation of the catalytically active Ni$_a$-S species. This hypothesis is in line with the broadening of the CO and CN stretching modes of HoxC$_{ai}$, which became more pronounced at low pH (Fig. 2C). This can be interpreted with Ni$_a$-S-related absorption bands underneath those of the prevailing Ni$_r$-S$_I$ and Ni$_r$-S$_{II}$ species.

Apart from explicit deviations in activity, HoxC, RH and preHoxG, and MBH also exhibit different HD/D$_2$ ratios (Table S7‡). While the HD production rate of HoxC is much higher than that of D$_2$, RH, preHoxG, and MBH show the opposite trend. This observation supports the assumption that the active site of HoxC lies in proximity to the protein surface (Fig. 1), resulting in a facilitated release of HD. In the case of preHoxG, the C-terminal extension may shield the catalytic center,[5] and in RH/MBH the active site is deeply buried within the holoenzyme.[35,60] This results in the retention of HD gas close to the active site, facilitating a second catalytic cycle, leading to the predominant formation of D$_2$.

It has been outlined before that at metal centers H$_2$ can compete both thermodynamically and kinetically with H$_2$O as a ligand, and the electrophilicity of a metal center must be just right to favor binding of H$_2$ over water.[61] Consequently, binding and processing of H$_2$ should be particularly easy at dedicated metal centers where the effective H$_2$O concentration is low. Thus, based on the peculiar biochemical and spectroscopic properties of HoxC, one important role of the small hydrogenase subunit seems to guarantee a hydrophobic environment of the catalytic center. This becomes evident when regarding the catalytic H/D exchange activity, which is independent of long-range electron transfer and, hence, should be independent of the electron-transfer capacity of the small subunit. Nevertheless, HoxC showed a 200-fold lower H/D exchange activity than native RH, suggesting a significantly increased competition between H$_2$ and H$_2$O for binding at the active site. Preventing water access to the active site and the resulting formation of oxidized states such as Ni$_r$-B is a prerequisite particularly for the H$_2$-sensing function of the RH, which needs to react immediately if H$_2$ is available.[17] The potential inhibitory role of water in catalysis should also be taken into account for chemical synthesis of [NiFe] mimics that are functional in aqueous solutions.[62]

Apart from active site protection, the small subunit is likely responsible for activating the catalytic center in a redox-dependent manner upon complex formation with the large subunit. We showed that HoxC$_{ai}$ is "locked" primarily in the Ni$_r$-S state(s) protecting the enzyme from redox inactivation. The presence of an OH$^-$/H$_2$O ligand in the bridging position between iron and nickel prevents interaction with H$_2$ and potentially harmful molecules such as CO and O$_2$ at physiological potential. This is particularly important for hydrogenase maturation under aerobic conditions as it occurs in *R. eutropha*.[63]

Conclusions

Our biochemical and spectroscopic investigations of the isolated large subunit HoxC of the regulatory [NiFe]-hydrogenase reveal that the catalytic center is equipped with stoichiometric amounts of nickel and iron and diatomic CN$^-$ and CO ligands coordinated to the latter. Moreover, the protein is capable of H$_2$ activation as shown by catalytic H/D exchange and methylene blue reduction measurements. The fact, that the HoxC activities were drastically lower compared to those of native RH may increase the possibility to trap early (short-lived) intermediates that have so far escaped from spectroscopic detection. For instance, exchanging presumably proton-accepting amino acid residues near the catalytic center, *e.g.* invariant glutamate and arginine residues,[64–66] could enable the identification of the proposed dihydrogen–metal sigma complex of the active site. Based on its distorted coordination within the active site, nickel is currently assumed to be the initial target of dihydrogen.[67] Corresponding experimental evidence, however, is not yet available.

Remarkably, HoxC retains the ability to split H$_2$ in the presence of molecular O$_2$, making it a companion of the isolated large subunit, preHoxG, of the membrane-bound [NiFe]-hydrogenase of *R. eutropha*.[5] To unravel whether this is a general feature, it is of high interest to isolate catalytically competent large subunits of O$_2$-sensitive [NiFe]-hydrogenases and to investigate their catalytic H/D exchange properties in the absence and presence of O$_2$. In fact, the premature large subunit, preHyhL, of the O$_2$-sensitive [NiFe]-hydrogenase of *Thermococcus kodakarensis* has already been isolated and its crystal structure was determined.[6] Intriguingly, the active site pocket revealed to be metal cofactor-free. Therefore, the RH large subunit, HoxC, represents thus far the best characterized miniaturized model of a [NiFe]-hydrogenase, and the biochemical and biophysical data presented in this study might be used as a benchmark to inspire chemists to synthetize well-performing biomimetic complexes that are able to split and produce H$_2$ under ambient conditions.

Conflicts of interest

There are no conflicts to declare.

Acknowledgements

Notes and references

1 D. Søndergaard, C. N. S. Pedersen and C. Greening, *Sci. Rep.*, 2016, **6**, 34212.

2 P. M. Vignais and B. Billoud, *Chem. Rev.*, 2007, **107**, 4206–4272.

3 G. Caserta, S. Roy, M. Atta, V. Artero and M. Fontecave, *Curr. Opin. Chem. Biol.*, 2015, **25**, 36–47.

4 W. Lubitz, H. Ogata, O. Rüdiger and E. Reijerse, *Chem. Rev.*, 2014, **114**, 4081–4148.

5 S. Hartmann, S. Frielingsdorf, A. Ciaccafava, C. Lorent, J. Fritsch, E. Siebert, J. Priebe, M. Haumann, I. Zebger and O. Lenz, *Biochemistry*, 2018, **57**, 5339–5349.

6 S. Kwon, S. Watanabe, Y. Nishitani, T. Kawashima, T. Kanai, H. Atomi and K. Miki, *Proc. Natl. Acad. Sci. U. S. A.*, 2018, **115**, 7045–7050.

7 C. Pinske, C. Thomas, K. Nutschan and R. G. Sawers, *Front. Microbiol.*, 2019, **10**, 2223.

8 L. Kleihues, O. Lenz, M. Bernhard, T. Buhrke and B. Friedrich, *J. Bacteriol.*, 2000, **182**, 2716–2724.

9 M. Brecht, M. van Gastel, T. Buhrke, B. Friedrich and W. Lubitz, *J. Am. Chem. Soc.*, 2003, **125**, 13075–13083.

10 M. Horch, J. Schoknecht, M. A. Mroginski, O. Lenz, P. Hildebrandt and I. Zebger, *J. Am. Chem. Soc.*, 2014, **136**, 9870–9873.

11 M. Horch, J. Schoknecht, S. L. D. Wrathall, G. M. Greetham, O. Lenz and N. T. Hunt, *Chem. Sci.*, 2019, **10**, 8981–8989.

12 P. A. Ash, J. Liu, N. Coutard, N. Heidary, M. Horch, I. Gudim, T. Simler, I. Zebger, O. Lenz and K. A. Vincent, *J. Phys. Chem. B*, 2015, **119**, 13807–13815.

13 F. Roncaroli, E. Bill, B. Friedrich, O. Lenz, W. Lubitz and M.-E. Pandelia, *Chem. Sci.*, 2015, **6**, 4495–4507.

14 Y. Ilina, C. Lorent, S. Katz, J.-H. Jeoung, S. Shima, M. Horch, I. Zebger and H. Dobbek, *Angew. Chem., Int. Ed.*, 2019, **58**, 18710–18714.

15 A. J. Pierik, M. Schmelz, O. Lenz, B. Friedrich and S. P. J. Albracht, *FEBS Lett.*, 1998, **438**, 231–235.

16 R. Hidalgo, P. A. Ash, A. J. Healy and K. A. Vincent, *Angew. Chem., Int. Ed.*, 2015, **54**, 7110–7113.

17 T. Buhrke, O. Lenz, N. Krauss and B. Friedrich, *J. Biol. Chem.*, 2005, **280**, 23791–23796.

18 G. Winter, T. Buhrke, O. Lenz, A. K. Jones, M. Forgber and B. Friedrich, *FEBS Lett.*, 2005, **579**, 4292–4296.

19 S. Löscher, I. Zebger, L. K. Andersen, P. Hildebrandt, W. Meyer-Klaucke and M. Haumann, *FEBS Lett.*, 2005, **579**, 4287–4291.

20 H. G. Podzuweit, K. Schneider and H. Knüttel, *BBA, Biochim. Biophys. Acta, Biomembr.*, 1987, **905**, 435–446.

21 S. Frielingsdorf, J. Fritsch, A. Schmidt, M. Hammer, J. Löwenstein, E. Siebert, V. Pelmenschikov, T. Jaenicke, J. Kalms, Y. Rippers, F. Lendzian, I. Zebger, C. Teutloff, M. Kaupp, R. Bittl, P. Hildebrandt, B. Friedrich, O. Lenz and P. Scheerer, *Nat. Chem. Biol.*, 2014, **10**, 378–385.

22 J. E. O'Reilly, *BBA, Biochim. Biophys. Acta, Bioenerg.*, 1973, **292**, 509–515.

23 P. Hosseinzadeh, N. M. Marshall, K. N. Chacón, Y. Yu, M. J. Nilges, S. Y. New, S. A. Tashkov, N. J. Blackburn and Y. Lu, *Proc. Natl. Acad. Sci. U. S. A.*, 2016, **113**, 262–267.

24 A. Volbeda, L. Martin, C. Cavazza, M. Matho, B. W. Faber, W. Roseboom, S. P. J. Albracht, E. Garcin, M. Rousset and J. C. Fontecilla-Camps, *J. Biol. Inorg. Chem.*, 2005, **10**, 239–249.

25 T. Yanai, D. P. Tew and N. C. Handy, *Chem. Phys. Lett.*, 2004, **393**, 51–57.

26 F. Weigend and R. Ahlrichs, *Phys. Chem. Chem. Phys.*, 2005, **7**, 3297.

27 M. J. Frisch, G. W. Trucks, H. B. Schlegel, G. E. Scuseria, M. A. Robb, J. R. Cheeseman, G. Scalmani, V. Barone, G. A. Petersson, H. Nakatsuji, X. Li, M. Caricato, A. V. Marenich, J. Bloino, B. G. Janesko, R. Gomperts, B. Mennucci, H. P. Hratchian, J. V. Ortiz, A. F. Izmaylov, J. L. Sonnenberg, D. Williams-Young, F. Ding, F. Lipparini, F. Egidi, J. Goings, B. Peng, A. Petrone, T. Henderson, D. Ranasinghe, V. G. Zakrzewski, J. Gao, N. Rega, G. Zheng, W. Liang, M. Hada, M. Ehara, K. Toyota, R. Fukuda, J. Hasegawa, M. Ishida, T. Nakajima, Y. Honda, O. Kitao, H. Nakai, T. Vreven, K. Throssell, J. A. Montgomery Jr, J. E. Peralta, F. Ogliaro, M. J. Bearpark, J. J. Heyd, E. N. Brothers, K. N. Kudin, V. N. Staroverov, T. A. Keith, R. Kobayashi, J. Normand, K. Raghavachari, A. P. Rendell, J. C. Burant, S. S. Iyengar, J. Tomasi, M. Cossi, J. M. Millam, M. Klene, C. Adamo, R. Cammi, J. W. Ochterski, R. L. Martin, K. Morokuma, O. Farkas, J. B. Foresman and D. J. Fox, *Gaussian 16, Revision A.03*, Gaussian, Inc., Wallingford CT, 2016.

28 V. Barone, M. Cossi and J. Tomasi, *J. Comput. Chem.*, 1998, **19**, 404–417.

29 S. Miertuš, E. Scrocco and J. Tomasi, *Chem. Phys.*, 1981, **55**, 117–129.

30 T. Simonson and D. Perahia, *Proc. Natl. Acad. Sci. U. S. A.*, 1995, **92**, 1082–1086.

31 C. Greco and L. De Gioia, *Inorg. Chem.*, 2011, **50**, 6987–6995.

32 M. K. Gilson and B. Honig, *Proteins: Struct., Funct., Genet.*, 1988, **4**, 7–18.

33 C. Greco, P. Fantucci, U. Ryde and L. de Gioia, *Int. J. Quantum Chem.*, 2011, **111**, 3949–3960.

34 A. L. De Lacey, V. M. Fernández, M. Rousset and R. Cammack, *Chem. Rev.*, 2007, **107**, 4304–4330.

35 T. Buhrke, S. Löscher, O. Lenz, E. Schlodder, I. Zebger, L. K. Andersen, P. Hildebrandt, W. Meyer-Klaucke, H. Dau, B. Friedrich and M. Haumann, *J. Biol. Chem.*, 2005, **280**, 19488–19495.

36 B. Bleijlevens, F. A. van Broekhuizen, A. L. De Lacey, W. Roseboom, V. M. Fernandez and S. P. J. Albracht, *J. Biol. Inorg. Chem.*, 2004, **9**, 743–752.

37 S. Kurkin, S. J. George, R. N. F. Thorneley and S. P. J. Albracht, *Biochemistry*, 2004, **43**, 6820–6831.

38 T. Krämer, M. Kampa, W. Lubitz, M. van Gastel and F. Neese, *ChemBioChem*, 2013, **14**, 1898–1905.

39 A. L. de Lacey, E. C. Hatchikian, A. Volbeda, M. Frey, J. C. Fontecilla-Camps and V. M. Fernandez, *J. Am. Chem. Soc.*, 1997, **119**, 7181–7189.

40 D. A. Fine, *Inorg. Chem.*, 1969, **8**, 1014–1016.

41 H. S. Shafaat, O. Rüdiger, H. Ogata and W. Lubitz, *BBA, Biochim. Biophys. Acta, Bioenerg.*, 2013, **1827**, 986–1002.

42 M.-E. Pandelia, H. Ogata and W. Lubitz, *ChemPhysChem*, 2010, **11**, 1127–1140.

43 S. P. J. Albracht, *BBA, Biochim. Biophys. Acta, Bioenerg.*, 1994, **1188**, 167–204.

44 H. Tai, Y. Higuchi and S. Hirota, *Dalton Trans.*, 2018, **47**, 4408–4423.

45 T. Yagi, M. Tsuda and H. Inokuchi, *J. Biochem.*, 1973, **73**, 1069–1081.

46 P. Vignais, *Coord. Chem. Rev.*, 2005, **249**, 1677–1690.

47 I. Bürstel, E. Siebert, G. Winter, P. Hummel, I. Zebger, B. Friedrich and O. Lenz, *J. Biol. Chem.*, 2012, **287**, 38845–38853.

48 M. Bernhard, T. Buhrke, B. Bleijlevens, A. L. De Lacey, V. M. Fernandez, S. P. J. Albracht and B. Friedrich, *J. Biol. Chem.*, 2001, **276**, 15592–15597.

49 W. V. Sweeney and J. C. Rabinowitz, *Annu. Rev. Biochem.*, 1980, **49**, 139–161.

50 D. Brazzolotto, M. Gennari, N. Queyriaux, T. R. Simmons, J. Pécaut, S. Demeshko, F. Meyer, M. Orio, V. Artero and C. Duboc, *Nat. Chem.*, 2016, **8**, 1054–1060.

51 Z. Li, Y. Ohki and K. Tatsumi, *J. Am. Chem. Soc.*, 2005, **127**, 8950–8951.

52 G. M. Chambers, M. T. Huynh, Y. Li, S. Hammes-Schiffer, T. B. Rauchfuss, E. Reijerse and W. Lubitz, *Inorg. Chem.*, 2016, **55**, 419–431.

53 H. Ogata, K. Nishikawa and W. Lubitz, *Nature*, 2015, **520**, 571–574.

54 M.-E. Pandelia, D. Bykov, R. Izsak, P. Infossi, M.-T. Giudici-Orticoni, E. Bill, F. Neese and W. Lubitz, *Proc. Natl. Acad. Sci. U. S. A.*, 2013, **110**, 483–488.

55 H. Tai, K. Nishikawa, M. Suzuki, Y. Higuchi and S. Hirota, *Angew. Chem., Int. Ed.*, 2014, **53**, 13817–13820.

56 N. Tamiya and S. L. Miller, *J. Biol. Chem.*, 1963, **238**, 2194–2198.

57 H. Tai, L. Xu, K. Nishikawa, Y. Higuchi and S. Hirota, *Chem. Commun.*, 2017, **53**, 10444–10447.

58 H. Tai, L. Xu, S. Inoue, K. Nishikawa, Y. Higuchi and S. Hirota, *Phys. Chem. Chem. Phys.*, 2016, **18**, 22025–22030.

59 M.-E. Pandelia, H. Ogata, L. J. Currell, M. Flores and W. Lubitz, *J. Biol. Inorg. Chem.*, 2009, **14**, 1227–1241.

60 J. Fritsch, P. Scheerer, S. Frielingsdorf, S. Kroschinsky, B. Friedrich, O. Lenz and C. M. T. Spahn, *Nature*, 2011, **479**, 249–252.

61 G. J. Kubas, *Chem. Rev.*, 2007, **107**, 4152–4205.

62 M. E. Ahmed, S. Chattopadhyay, L. Wang, D. Brazzolotto, D. Pramanik, D. Aldakov, J. Fize, A. Morozan, M. Gennari, C. Duboc, A. Dey and V. Artero, *Angew. Chem., Int. Ed.*, 2018, **57**, 16001–16004.

63 *Biohydrogen*, ed. M. Rögner, De Gruyter, Berlin, München, Boston, 2015.

64 R. M. Evans, E. J. Brooke, S. A. M. Wehlin, E. Nomerotskaia, F. Sargent, S. B. Carr, S. E. V. Phillips and F. A. Armstrong, *Nat. Chem. Biol.*, 2016, **12**, 46–50.

65 R. M. Evans, P. A. Ash, S. E. Beaton, E. J. Brooke, K. A. Vincent, S. B. Carr and F. A. Armstrong, *J. Am. Chem. Soc.*, 2018, **140**, 10208–10220.

66 S. Dementin, B. Burlat, A. L. De Lacey, A. Pardo, G. Adryanczyk-Perrier, B. Guigliarelli, V. M. Fernandez and M. Rousset, *J. Biol. Chem.*, 2004, **279**, 10508–10513.

67 M. Bruschi, M. Tiberti, A. Guerra and L. De Gioia, *J. Am. Chem. Soc.*, 2014, **136**, 1803–1814.